



# Thinnest npn homojunction for inspired photoelectrochemical water splitting

Xiaodong Wang<sup>a,1</sup>, Xiaoqing Liu<sup>b,1</sup>, Yu Wu<sup>a</sup>, Yaling Fu<sup>a</sup>, Huijuan Zhang<sup>a</sup>, Miao Zhou<sup>b</sup>, Yu Wang<sup>a,c,\*</sup>

<sup>a</sup> The School of Chemistry and Chemical Engineering, State Key Laboratory of Power Transmission Equipment & System Security and New Technology, Chongqing University, 174 Shazheng Street, Shapingba District, Chongqing City 400044, PR China

<sup>b</sup> The School of Optoelectronic Engineering Key Laboratory of Optoelectronic Technology and System of Ministry of Education, Chongqing University, Chongqing 400044, PR China

<sup>c</sup> The School of Electrical Engineering, Chongqing University, 174 Shazheng Street, Shapingba District, Chongqing City, 400044, PR China

## ARTICLE INFO

### Keywords:

Thinnest npn homojunction  
Sb doping  
Photoelectrochemical water splitting

## ABSTRACT

Tin monosulfide semiconductors have great potential for a wide range of applications related to solar energy conversion, however, the photoelectrochemical water splitting performance and stability of tin monosulfide are still inferior. To bridge the gap, effective strategies should be developed to optimize tin monosulfide semiconductors. Here, we report for the first time the thinnest sandwiched SnS n-p-n homojunction regulated by Sb doping and Sn vacancies (npn-SnS). Experimental observations and density functional theory calculations reveal that Sb doping and Sn vacancies form a bidirectional built-in electric field that can enhance the separation and transport efficiency of carriers. Due to the interaction between Sb and S, the thickness of npn-SnS is only 1.69 nm, and defect-related recombination is suppressed after Sb doping. As a result, the photocurrent density of the ultrathin npn-SnS photocathode is  $3.3 \text{ mA cm}^{-2}$ , which is 4 times higher than that of p-SnS (containing Sn vacancies) and surpasses all SnS-based photocathodes reported so far. This work synthesizes the thinnest sandwiched n-p-n homojunction, which can serve as a guide for improving the carrier separation efficiency and stability of other semiconductors.

## 1. Introduction

Photoelectrochemical (PEC) or electrochemical water splitting can provide a feasible method to convert solar or electrical energy into chemical energy that can be transported and consumed arbitrarily with negligible impact on the environment [1–7]. To use chemical fuel products, water-splitting photoelectrodes are required to construct PEC systems for efficient photo-induced energy conversion [8]. Tremendous efforts are devoted to developing semiconductors with high photo-conversion efficiency. Despite these efforts, the efficiency of modern photoelectrodes remains relatively low, which limits the overall efficiency of PEC water splitting [9]. Shape modulation of semiconductor nanostructures has advanced rapidly over the past few decades, as control over shape introduces new optical [10,11], electronic [12], and assembly properties [13] to these complex nanostructures. In particular,

low-dimensional surface science has entered a new era with the isolation of graphene [14,15]. However, the stupendous potential of the monochalcogenides (SnS, SnSe, etc.) remains unexplored. Theoretical studies of these materials have revealed their peculiar electronic and optoelectronic properties in the low-dimensional limit, but have not gained a large experimental thrust due to poor performance and structural instability [16,17].

SnS is a representative member of the family of post-transition metal monochalcogenides and exists in an orthorhombic layered structure [18, 19]. Bulk SnS is held by van der Waals (vdW) forces and exhibits structural anisotropy between layers, a feature very similar to the isolectronic structure of black phosphorus (BP) [20]. The tunable band gap endows it with desirable electronic and optoelectronic properties, including decent absorption efficiency, desirable electrical conductivity [21], and high electron mobility [22]. To date, there are few studies on

\* Corresponding author at: The School of Chemistry and Chemical Engineering, State Key Laboratory of Power Transmission Equipment & System Security and New Technology, Chongqing University, 174 Shazheng Street, Shapingba District, Chongqing City 400044, PR China.

E-mail address: [wangy@cqu.edu.cn](mailto:wangy@cqu.edu.cn) (Y. Wang).

<sup>1</sup> These authors contributed equally to this work.

<https://doi.org/10.1016/j.apcatb.2022.122182>

Received 14 August 2022; Received in revised form 9 November 2022; Accepted 12 November 2022

Available online 14 November 2022

0926-3373/© 2022 Elsevier B.V. All rights reserved.

atomic-scale SnS nanosheets. Xie et al. firstly reported monolayer chalcogenide nanosheets, which exhibit excellent atom utilization and PEC performance, but poor stability [23]. Walia et al. reported ultrathin SnS layers through printing liquid metal tin. Thicknesses vary from single-cell to multi-cell, exhibiting a broad wavelength response from UV to IR. Nevertheless, the synthesis process is cumbersome and thickness is difficult to control [24]. The easy oxidation of  $\text{Sn}^{2+}$  can form Sn vacancies in the photocathode films, leading to defect-related recombination and greatly reducing the conversion efficiency [25]. Many studies reported improving the performance of SnS by doping Cu [26], Sb [27], or In/Sb [28]. However, the thickness of the synthesized SnS is generally several hundred nanometers, which will cause serious carrier recombination. In addition, S-rich synthesis conditions should be chosen to avoid deep trap states derived from S vacancies (Vs) or Sn-on-S anti-defects, and conversely, sulfur must be controlled at low levels to prevent the formation of secondary phases [29]. Therefore, an optimized strategy needs to be proposed to avoid the above problems. To our knowledge, there is no report on the synthesis of the thinnest npn-structured SnS homojunction.

Here, we synthesized the thinnest three-layer SnS for the first time and doped the outer layer with Sb to form an npn homojunction. Sb-doping and S-vacancies constitute a built-in electric field that accelerates the separation/transport of electrons and holes. Meanwhile, the interaction of S atoms and Sb atoms in SnS shortens the interlayer distance, thereby improving the stability. The experimental results reveal that the defect-related recombination is effectively suppressed by Sb-doping, and the true atom-thick material still maintains the original structure. The photocurrent density of npn-SnS is  $3.3 \text{ mA cm}^{-2}$  at 0 V versus reversible hydrogen electrode ( $\text{V}_{\text{RHE}}$ ). We also found that the photocurrent of the ultrathin interlayer npn-SnS remains stable for 21 h and has an IPCE value of 73 % at 430 nm, surpassing all SnS-based photocathodes. Furthermore, the theoretical results confirm that S-vacancies and Sb-doping indeed form a built-in electric field that enhances the water splitting performance. The novel design and fabrication of atomically thin npn-SnS provides a promising route for PEC water splitting.

## 2. Experimental

### 2.1. Chemical and materials

The following chemicals and materials were used in this work: acetone ( $\text{C}_3\text{H}_6\text{O}$ ), ethanol ( $\text{C}_2\text{H}_6\text{O}$ ), stannous chloride dihydrate ( $\text{SnCl}_2 \cdot 2\text{H}_2\text{O}$ ), thiourea ( $\text{CH}_4\text{N}_2\text{S}$ ), ammonium sulfide ( $(\text{NH}_4)_2\text{S}$ ), ethylene glycol ( $\text{C}_2\text{H}_6\text{O}_2$ ) and citric acid ( $\text{C}_6\text{H}_8\text{O}_7$ ) were purchased from Chengdu Cologne Chemicals Co., Ltd. Antimony chloride ( $\text{SbCl}_3$ ) was purchased from Shanghai Macklin Biochemical Co., Ltd. During the whole experimental process, deionized water was provided as water. Conductive fluorine-doped tin oxide (FTO,  $1.6 \times 20 \times 30 \text{ mm}$ ) glass was used as all working electrodes.

### 2.2. Synthesis of p-type SnS (p-SnS) nanosheet photocathodes

The FTO conductive glass substrates were sonicated with acetone, ethanol, and deionized water for 30 min, and then dried for use. During the synthesis process, 0.2256 g  $\text{SnCl}_2 \cdot 0.2 \text{ H}_2\text{O}$  and 0.2284 g  $\text{CH}_4\text{N}_2\text{S}$  (TAA) were mixed, then added to 30 mL of ethylene glycol, and magnetic stirring was continued for 30 min until completely dissolved. Subsequently, 0.1921 g of citric acid was added and the mixture was magnetically stirred well for 10 min. Add 8  $\mu\text{L}$   $(\text{NH}_4)_2\text{S}$  dropwise to the above clear solution and continue magnetic stirring for 10 min. Divide the above solution into 5 mL portions and add them to a 50 mL Teflon-lined stainless steel autoclave along with clean FTO conductive glass (with the conductive side of the FTO facing down). They were then kept at  $180^\circ\text{C}$  for 16 h. After naturally cooling to room temperature, the FTO conductive glass with the samples was carefully taken out, repeatedly

washed with deionized water and ethanol, and vacuum dried at  $50^\circ\text{C}$  overnight for the next characterization and experiment. Furthermore, we tune the Sn vacancies in p-SnS by changing the quality of the precursor  $\text{SnCl}_2 \cdot 0.2 \text{ H}_2\text{O}$ .

### 2.3. Fabrication of npn-SnS nanosheet photocathodes

First, the prepared p-SnS nanosheet photocathode was placed downstream of the tube furnace. Then, 0.2281 g of  $\text{SbCl}_3$  powder was placed at the bottom of a glass test tube placed upstream of the tube furnace with the opening facing the p-SnS nanosheet photocathode. Subsequently, the reaction system was evacuated with argon (Ar) for a sufficient time and the Ar flow rate was controlled at  $60 \text{ mL min}^{-1}$ . Finally, heat the tube furnace to  $250^\circ\text{C}$  at a heating rate of  $5^\circ\text{C min}^{-1}$ . When the temperature reaches  $250^\circ\text{C}$ , reduce the Ar flow rate to  $40 \text{ mL min}^{-1}$  while maintaining the temperature for 5 min. After the reaction, the system was naturally cooled to room temperature, and the npn-SnS photocathode was carefully taken out for further characterization tests. Furthermore, we control the doping amount of Sb by changing the flow rate of Ar when the temperature reaches  $250^\circ\text{C}$ .

### 2.4. Characterization

The morphology and microstructure of the samples were characterized by field emission scanning electron microscopy (FESEM; JEOL-7800F) and transmission electron microscopy (TEM; FEI Talos F200X). Energy dispersive X-ray (EDX) spectroscopy elemental mapping was conducted under the TEM with an annular dark-field (ADF) detector. The thickness of samples was measured by atomic force microscopy (AFM, MFP-3D-BIO, Asylum Research Inc, USA). The powder X-ray diffractometer (XRD, PANalytical X'Pert Powder with Cu  $\text{K}\alpha$  radiation), a Raman spectrometer equipped with an argon (532 nm) laser to cover the wavenumber range of  $100\text{--}2000 \text{ cm}^{-1}$  (Horiba LabRAM HR Evolution), and an X-ray photoelectron spectrometer (XPS) with an ESCALAB 250Xi from Thermo Fisher Scientific using monochromatic Al  $\text{K}\alpha$  radiation (225 W, 15 mA, 15 kV), an Inductively coupled plasma atomic emission spectrometry (ICP-AES) with an Atomscan Advantage (Thermo Jarrell Ash Corporation (USA)), were adopted to characterize the as-prepared samples. A UV-visible (UV-vis) spectrophotometer (UV-3600, SHIMADU, JAPAN) was used to record the ultraviolet-visible diffused reflectance spectra (UV-vis DRS). Ultraviolet photoemission spectroscopy (UPS) measurements were carried out on an ESCA LAB 250 Xi spectrometer with He I resonance lines (21.2 eV). The steady-state photoluminescence (PL) spectra (excited by 370 nm illumination) and were recorded on a spectrofluorometer (FLS1000, Edinburgh Instruments) equipped with both continuous (450 W) and pulsed xenon lamps. The time-resolved transient photoluminescence decay (TRPL) spectra were recorded on a spectrophotometer (Fluorolog-3, Horiba Scientific) with 450 W xenon lamp. The surface photovoltaic properties (SPV) of samples were tested by a surface photovoltage test system (CEL-SPS1000).

### 2.5. PEC water splitting performance tests

The PEC performance measurements of the samples were carried out in a 150 mL controllable reaction system (CEL-PAEM-D8, CEAULight, China). Before testing, bubbling high-purity Ar into electrolyte solution for 30 min at room temperature to remove  $\text{O}_2$ . A commercial solar simulator (S500RE7, CEAULight, China) with a light intensity (1 sun at AM 1.5 G) of  $100 \text{ mW cm}^{-2}$  was used to illuminate the photocathode. CHI 760E as the workstation and 0.5 M  $\text{Na}_2\text{SO}_4$  (PH 6.82) as the electrolyte, a series of PEC performance tests were carried out. Ag/AgCl and carbon rod were used as the reference and counter electrode, the as-prepared samples were used as the working electrodes respectively. Using a scan rate of  $5 \text{ mV s}^{-1}$  and under illumination to measure J-V. All obtained potentials (vs. Ag/AgCl) were converted to reversible

hydrogen electrodes (RHE) according to the Nernst equation:

$$E_{\text{RHE}} = E_{\text{Ag/AgCl}} + 0.059 \text{ pH} + E^{\circ}_{\text{Ag/AgCl}}$$

where  $E^{\circ}_{\text{Ag/AgCl}} = 0.1976 \text{ V}$  at  $25^{\circ}\text{C}$  and  $E_{\text{Ag/AgCl}}$  is the experimentally measured potential versus the Ag/AgCl reference.

Meanwhile, the stability I-T test was recorded under the illumination at  $0.0 \text{ V}_{\text{RHE}}$ . Electrochemical impedance spectra (EIS) were recorded in a three-electrode system under light illumination, with the frequency ranging from  $0.01 \text{ Hz}$  to  $100 \text{ kHz}$ . The Mott-Schottky (M-S) plots were acquired under the dark condition with a frequency of  $1.0 \text{ kHz}$  and amplitude of  $0.01 \text{ V}$ . The incident photon to current efficiency (IPCE) was measured under monochromatic irradiation from a Xe lamp equipped with bandpass filters. The IPCE for each wavelength is determined by the following formula:

$$\text{IPCE} = (1240 \text{ J}) / (\lambda I_{\text{light}}) \times 100 \%$$

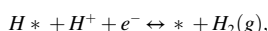
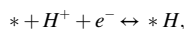
Where  $\lambda$  is the wavelength of incident light (nm),  $J$  is the photocurrent density ( $\text{mA cm}^{-2}$ ) under illumination of wavelength ( $\lambda$ ),  $I_{\text{light}}$  is the incident intensity of incident light ( $\text{mW cm}^{-2}$ ). The gas was detected by gas chromatography (AulightGC-7920) equipped with a thermal conductivity detector (TCD) and flame ionization detector (FID).

## 2.6. Computational details

Density function theory based first-principles calculations were accomplished with the projector augmented wave (PAW) formalism as implemented in the Vienna ab initio simulation package (VASP)[30,31]. The electronic exchange-correlation energy was treated by generalized gradient approximation of Perdew–Burke–Ernzerhof (GGA-PBE) [32]. A  $3 \times 3 \times 1$  SnS supercell containing 36 atoms was used to represent the pure structure. The Sn-vacancy SnS was formed by a single Sn atom removed from the pure SnS monolayer, while the Sb-doping structure is created by using a single Sb atom to replace Sn atom. Furthermore, the effect of van der Waals (vdW) interaction in heterojunctions is accounted for by using the correction method proposed by J. Klimeš (optPBE-vdW) [33]. This npn-SnS supercell contained 107 atoms of three single SnS monolayers, consisting of Sb-doping (1st layer), Sn-vacancy (2nd layer) and Sb-doping (3rd layer) SnS layers, respectively. Here, a vacuum layer thickness of  $20 \text{ Å}$  is employed for npn-SnS to avoid layer-to-layer interaction. The plane-wave basis of energy cutoff is  $400 \text{ eV}$ . A k-point mesh of  $3 \times 3 \times 1$  and  $7 \times 7 \times 1$   $\Gamma$ -centered grids in the first Brillouin zone was sampled for the structural optimization energy and electronic structure calculations, respectively. The convergence criteria of energy and forces were  $10^{-5} \text{ eV}$  and  $0.03 \text{ eV/Å}^{-1}$ , respectively. Ab initio molecular dynamics (MD) simulations were performed for  $5 \text{ ps}$  with a time step of  $1 \text{ fs}$  for npn-SnS. The constant amount of substance (N), volume (V), and temperature (T) canonical ensemble (NVT) was used by the algorithm of Nosé thermostat [34]. To calculate the Gibbs free energy difference ( $\Delta G$ ) in HERs by using the method of Nørskov et al. [35–38], which can be calculated as,

$$\Delta G = \Delta E + \Delta E_{\text{zpe}} - T\Delta S + \Delta G_{\text{pH}},$$

where  $\Delta E$  is the difference of each reaction (electronic) energy by the DFT computation.  $\Delta E_{\text{zpe}}$  represents the zero-point energy difference. For each step,  $E_{\text{zpe}} = 1/2 \sum \hbar \nu$  for each adsorbate and free molecules are vibrational frequencies overall normal modes  $\nu$ .  $T = 298.15 \text{ K}$  in this work and  $\Delta S$  represents the entropy difference that the entropies (S) of the free hydrogen molecule can be found from the NIST database [39]. Moreover,  $\Delta G_{\text{pH}} = 0.059 \times \text{pH}$  is the free-energy contribution due to the variations in H concentration. The HER process includes two-electron steps that can be expressed as,



The free energy difference for HER electrochemical step can be expressed as,

$$\Delta G^* = G^* - \frac{1}{2} G_{\text{H}_2} + \Delta G_{\text{pH}}.$$

## 3. Results and discussion

### 3.1. Synthesis and characterization of the npn-SnS

The simplified fabrication processes of p-SnS (Sn-vacancies only) and npn-SnS nanosheets (Sb-doping and Sn-vacancies) are shown in Fig. 1a. Three-cell-unit p-SnS grown vertically on FTO was synthesized by hydrothermal method at  $180^{\circ}\text{C}$ . Then, p-SnS was treated with Ar gas containing  $\text{Sb}^{2+}$  to obtain npn-SnS. Atomic force microscopy (AFM) images of p-SnS and npn-SnS reveal that npn-SnS is thinner than p-SnS (Figs. S1, 2), which may be attributed to the attraction of S to Sb (see XPS analysis below). We also synthesized materials with varying amounts of Sb-doping and Sn-vacancies (Figs. S3, 4). The results manifest that the morphologies of p-SnS and npn-SnS remain unchanged even though the Sn-vacancies and Sb-doping contents are changed. Inductive coupled plasma emission spectrometer (ICP) results show that the ratio of Sn to S in p-SnS is less than 1, thus indicating the existence of Sn-vacancies in p-SnS (Table S1) [21]. To further confirm that the different layers of npn-SnS contain vacancies and doping, we sonicated npn-SnS for  $30 \text{ min}$  to obtain monolayers. High-resolution transmission electron microscopy (HRTEM) and intensity distribution confirm the existence of Sn-vacancies (Fig. S5a, c). In contrast, the lattice of the Sb-doped layer becomes more complete, and the intensity profile also illustrates no vacancy defects, indicating that Sb has been successfully doped into npn-SnS (Fig. S5b, d). Ultrathin npn-SnS nanosheets with a vertical height of about  $600 \text{ nm}$  are sequentially grown on a substrate (FTO) (Fig. 1b). HRTEM images show that the lattice spacing of npn-SnS is about  $0.291 \text{ nm}$  (Fig. 1c), which corresponds exactly to the  $d_{101}$  of SnS, and the corresponding  $88^{\circ}$  dihedral angle is in good agreement with the angle between the (101) and ( $-101$ ) planes in orthorhombic SnS [23]. The structural information of p-SnS and npn-SnS nanosheets was revealed by X-ray diffraction (XRD). p-SnS and npn-SnS remain highly crystalline, indicating that vacancies or doping do not change the orthorhombic structure (Fig. S6a, JCPDS No. 083–1758). Raman spectroscopy was used to study the phase information of p-SnS and npn-SnS (Fig. S6b). Raman spectroscopy results demonstrate that the peak positions of p-SnS and npn-SnS are very close, and almost all of these peaks are assigned to SnS [40]. In addition, the peaks of npn-SnS change slightly after Sb doping, which indicate that Sb is incorporated into SnS instead of forming an impurity phase [15]. Transmission electron microscopy (TEM) reveals that npn-SnS has an ultrathin and transparent nanosheet structure (Fig. 1d). Furthermore, the lateral HRTEM image of npn-SnS reveals that the average height of npn-SnS is  $1.69 \text{ nm}$  (inset in Fig. 1d), which matches well with the thickness along the [010] direction. Combining the results of AFM and lateral HRTEM can confirm that npn-SnS is thinner than p-SnS, resulting in a compact structure and improved stability. Fig. S7 shows that almost all npn-SnS photocathodes are three-unit-cell thick, which is close to that of three-unit-cell SnS along the [010] direction (Fig. S8). High-angle annular dark-field scanning transmission electron microscopy (HAADF-STEM) images and elemental mapping of lateral npn-SnS nanosheets show that Sb is distributed in the outer layer, while S and Sn are uniformly distributed in the nanosheets, indicating successful construction of npn homojunction (Fig. 1e). We employ ICP tests to further demonstrate that Sb atoms have been successfully doped in npn-SnS. As displayed in Table S2, Sb was present in each sample in an amount ranging from  $0.3 \%$ – $2.8 \%$  in npn-SnS.

The compositions and valence states of p-SnS and npn-SnS were obtained by X-ray photoelectron spectroscopy (XPS). The S 2p core level spectra of p-SnS and npn-SnS show a spin-orbit splitting of  $\sim 1.1 \text{ eV}$ , and



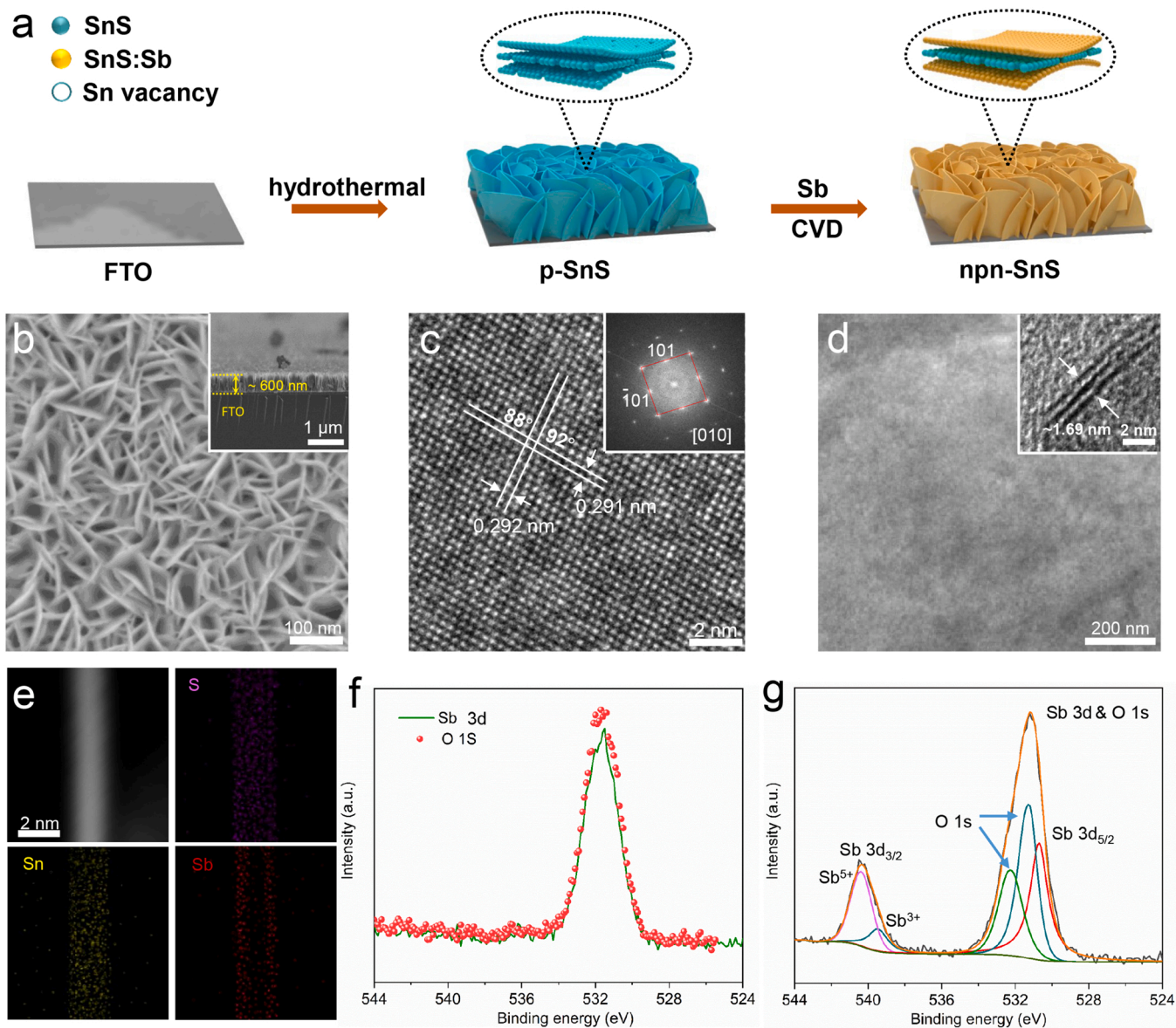


**Fig. 1.** a) Schematic illustration of the synthesis of p-SnS and npn-SnS. b) SEM image of npn-SnS. c) HRTEM image and corresponding FFT pattern of npn-SnS. d) TEM and lateral HRTEM image (inset) of npn-SnS. e) HAADF-STEM image and the corresponding EDS elemental mapping of npn-SnS. High-resolution XPS spectra of Sb 3d and O1s for f) p-SnS. g) npn-SnS.

the S 2p spectra show only one chemical interaction, where the peaks at 161.7 eV, 162.8 eV for p-SnS and 161.6 eV, 162.7 eV for npn-SnS correspond to the 2p<sub>3/2</sub> S and 2p<sub>1/2</sub> spin states of Sn-S (Fig. S9a) [23,41]. Notably, the binding energy of sulfur in p-SnS is higher than that in npn-SnS. This observation suggests that S gets electrons from other atoms [42]. Furthermore, the Sn 3d core level spectra of p-SnS and npn-SnS show a spin-orbit splitting of ~8.4 eV. The peak positions at 487.3, 495.8 eV, and 487.3, 495.7 eV are related to the Sn 3d<sub>5/2</sub> and Sn 3d<sub>3/2</sub> spin states of Sn-S (Fig. S9b) [40,41]. It is worth noting that even when Sb is doped into SnS, the binding energy change of S-Sn is almost negligible. The p-SnS has a peak at 531.3 eV (Fig. 1f, g), possibly corresponding to the O 1s peak [43]. However, a peak at 531.2 eV was also observed in the spectrum of npn-SnS. Combining the above results, we can infer that the peak at 531.2 eV of npn-SnS is related to Sb 3d<sub>5/2</sub> or O 1s, while the peak at 540.4 eV can prove the successful doping of Sb into p-SnS [44,45]. Furthermore, the peak at 540.4 eV can be deconvoluted into Sb<sup>3+</sup> (539.5 eV) and Sb<sup>5+</sup> (540.4 eV). This result indicates that the valence electrons of Sb doped in npn-SnS are attracted by other atoms. Combined with the previous literature, it can be proved that the

electrons of Sb are transferred to S atoms [42].

### 3.2. Band gap structure of the npn-SnS

The absorption properties and  $E_g$  of p-SnS and npn-SnS were evaluated through ultraviolet-visible diffuse reflectance spectroscopy (UV-vis) and corresponding Tauc plots. The band gap of p-SnS is 1.40 eV, and the  $E_g$  of npn-SnS is narrower (1.36 eV), consistent with the previous value [46], which proves that Sb doping indeed narrows the band gap and improves the light absorption ability (Fig. S10a, b and S11a). M-S measurements were employed to confirm the conductivity type of npn-SnS (Fig. 2a and Fig. S11b). Due to Sn vacancies and Sb doping, the M-S plot presents linear lines with negative and positive slopes at different potential regimes, indicating the existence of p-type and n-type features in npn-SnS [47]. Meanwhile, the Fermi level ( $E_F$ ) of npn-SnS is determined by extrapolation of the abscissa, and the Fermi levels of the outer and inner layers are denoted as  $E_{Fn}$  and  $E_{Fp}$ , respectively. In addition, the  $E_{Fp}$  of p-SnS is close to that of npn-SnS (Fig. S12), given the previous reports, we can infer that the  $E_{Fp}$  of p-SnS can

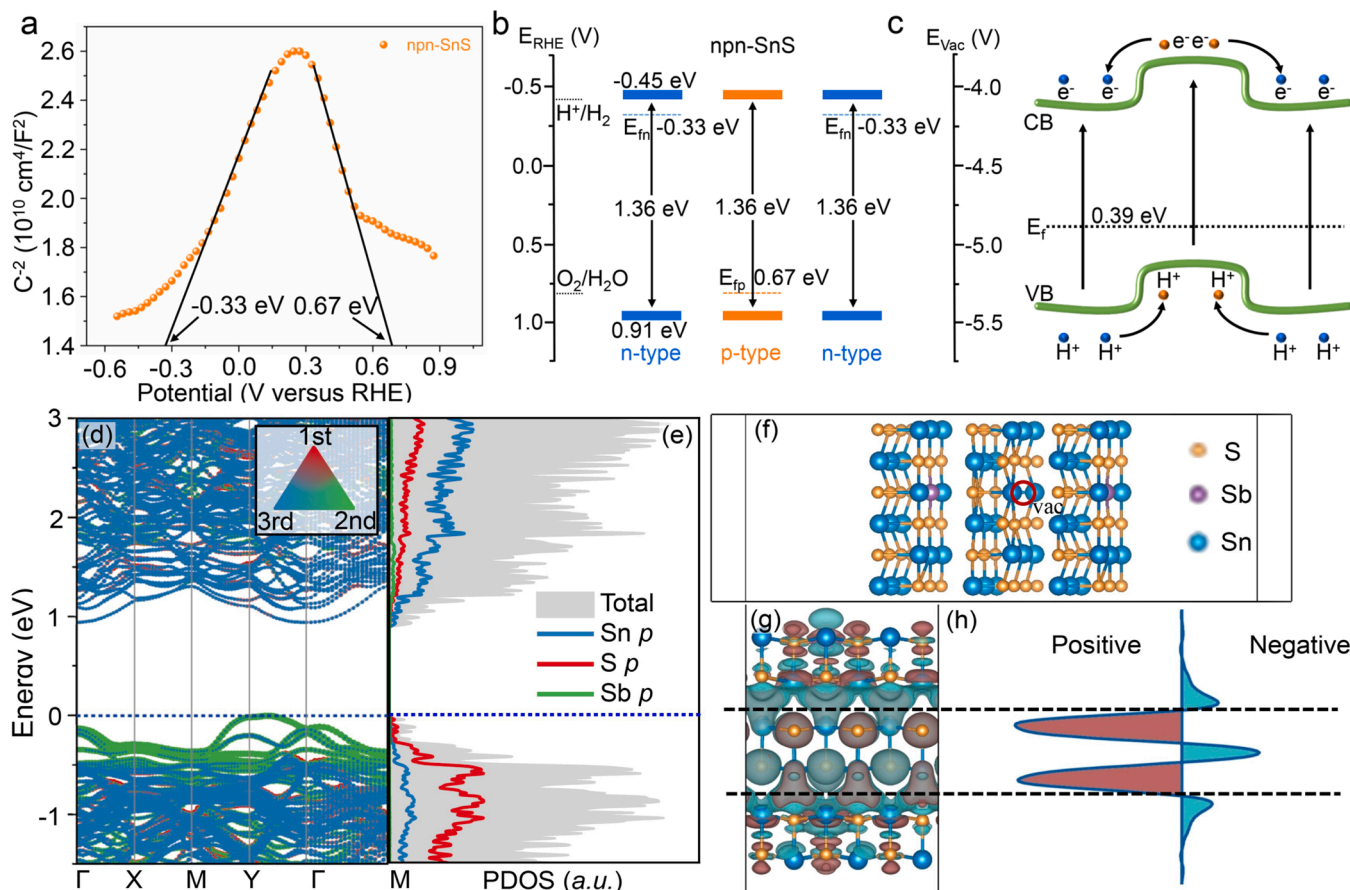


**Fig. 2.** a) M-S plot of npn-SnS. b) Illustration of npn-SnS band structure and water redox potential. c) sketch for carriers transfer of npn-SnS (CB= conduction band, VB= valence band). d) band structures. e) projected density of state (PDOS). f) the geometry structure. g) The charge density difference and h) the average difference electron density that is perpendicular to the XZ plane of npn-SnS.

represent npn-SnS to a certain extent [48]. Employing ultraviolet photoelectron spectroscopy (UPS) measurements to investigate the band structure of npn-SnS. The cut-off energies ( $E_{\text{cutoff}}$ ) of p-SnS and npn-SnS are 16.07 eV and 16.31 eV, respectively. The work functions of npn-SnS and p-SnS were determined by subtracting the cutoff energy ( $E_{\text{cutoff}}$ ) of the secondary electrons from the He I excitation energy (21.2 eV). The position of the valence band maximum relative to the Fermi level was obtained from the onset valence band photoemission on the low binding energy edge of the UPS spectrum [9]. The detailed band structure obtained from the UV-vis, UPS, and M-S data of npn-SnS are shown in Fig. 2b, and the band positions of p-SnS and npn-SnS are listed in Table S5. The npn-SnS photocathode can split water because the band structure strides the redox potential of water. The presence of p-type and n-type properties in npn-SnS favors the formation of n-p-n homojunction, and the alignment of the new  $E_F$  creates a built-in electric field that promotes efficient separation and transfer of electron-hole pairs (Fig. 2c). Electrochemical impedance spectroscopy (EIS) tests were performed under illumination to investigate the charge transport properties at the npn-SnS interface (Fig. S13). The significantly lower resistance of npn-SnS, suggests the improved PEC water splitting efficiency.

To construct a reasonable npn-SnS homojunction, the geometric and electronic structures for the supercells for pure SnS, Sn-vacancy SnS, and Sb doping (replace Sn) are displayed in Fig. S14 a-c. The optimized lattice constants of  $3 \times 3 \times 1$  supercell are  $a = 12.35 \text{ \AA}$ ,  $c = 12.66 \text{ \AA}$  (4.12  $\text{\AA}$  and 4.22  $\text{\AA}$  for primitive cell). As shown in Fig. S14 d-f, the pure SnS monolayer has an indirect band gap of 1.47 eV, consistent with the previous reports [49]. The Sb-doping and Sn-vacancy SnS also have indirect band gaps of 1.36 eV and 1.38 eV, respectively. The VBM and CBM are located at the middle of the  $\Gamma$ -Y and  $\Gamma$ -X points for the three

systems, respectively. Surprisingly, the Fermi level of Sn-vacancy SnS moved to the valence band, indicating the characteristics of p-type. In addition, the npn-SnS is an n-type semiconductor cause the Fermi level shift to the conduction band [50]. From the projected density of state (PDOS) in Fig. S15, we find that  $p$  orbital of S and  $p$  orbital of Sn contribute to the VBM and the CBM, respectively, for three structures.

Here, we constructed an npn-SnS model as depicted in Fig. 2f, which consists of Sb-doping (1st layer), Sn-vacancy (2nd layer), and Sb-doping (3rd layer) SnS layers, respectively. After optimization, the thickness [010] of the npn-SnS is 14.74  $\text{\AA}$ . The ab initio MD simulations were conducted to investigate the thermodynamic stability of npn-SnS at room temperature ( $T = 300 \text{ K}$ ). It is found that the total energy fluctuates slightly around a fixed value within the simulation's time, except for some miscellaneous peaks, and the temperature changes near 300 K (Fig. S16). No structural deformation was observed during the whole period of simulation, demonstrating that npn-SnS have stable thermodynamic stability. As displayed in Fig. 2d, the VBM of the inside layer (2nd) is near the Fermi level, showing a p-type property, which is consistent with the Sn-vacancy SnS monolayer. Additionally, the CBM of the two outside layers (1st, 3rd layer) is close to the Fermi level (relative to the inside layer), indicating the n-type property with the same as the Sb-doping SnS layer. Therefore, the modified three-layer SnS constructed an npn homojunction (npn-SnS). According to the corresponding PDOS of npn-SnS from Fig. 2e, the VBM near the  $E_F$  is contributed by  $p$ -orbitals of S atom, while the CBM is donated by the Sn, S, and Sb atoms. From the charge density difference and average difference electron density analysis as shown in Fig. 2g-h, the electron transfer from the 1st and 3rd layers to the 2nd layer and gather in the Sn-vacancy layer. By Bader analysis (Table S6), it can draw a conclusion



that the 2nd layer receives a charge of  $0.96e^-$  and the 1st and 3rd lose  $0.49$  and  $0.59e^-$ , respectively. Thus, a bidirectional built-in electric field was formed which is orientated from the 1st and 3rd layer to the 2nd layer. The bidirectional built-in electric field can effectively suppress the regenerative recombination of carriers. Collectively, these theoretical calculations also indicate that the three-layer systems present an npn homogeneous junction (nnpn-SnS), which would facilitate electron-hole pairs separation/transport efficiency during PEC tests.

### 3.3. Reaction mechanism and performance testing

Fig. 3a illustrates the internal structure of npn-SnS and its brief mechanism for water splitting. It can be seen that the built-in electric field improves the carrier separation and transport efficiency due to the existence of Sn vacancies and Sb doping. To further justify Fig. 3a and explain the source of the excellent PEC water-splitting activity, various spectroscopic measurements were performed. The photoluminescence (PL) emission spectra of the different samples are shown in Fig. S17a. The intensity of the PL emission spectrum is significantly reduced after Sb doping, indicating that the built-in electric field can facilitate the separation of photogenerated charges. Importantly, p-SnS displays two peaks at  $\sim 649.7$  and  $\sim 715.5$  nm, which may be attributed to the recombination of deep trap states induced by Vs/Sn-on-S antisite defects or defect-related recombination induced by Sn vacancies. Although there is no report on the origin of these two absorption peaks, experimental and theoretical studies of  $Ta_3N_5$  suggest that the sub-bandgap optical absorption is caused by defects[51]. Indeed, the defect-related emission peaks are significantly suppressed after Sb doping, indicating that Sb doping can effectively eliminate defects in p-SnS. The surface photovoltaic (SPV) spectral signal of npn-SnS is significantly increased relative to that of p-SnS, indicating accelerated carrier separation/-transfer of npn-SnS (Fig. S17b). The negative signals of p-SnS and npn-SnS imply that charges can be transferred to the surface under illumination. To gain further insight into the carrier dynamics of p-SnS and npn-SnS, time-resolved PL (TRPL) spectroscopy was employed (Fig. 3b).  $\tau_1$  is ascribed to defect-related photogenerated carrier trapping, while  $\tau_2$  is due to electron-hole recombination from the conduction band to the valence band[9]. The PL decay of the p-SnS film is mainly caused by defect-related recombination (41.15 %), and the lifetime is only 0.78 ns. On the contrary, both  $\tau_1$  and  $\tau_2$  of npn-SnS became longer, and the defect-related recombination rate decreased (18.75 %), indicating that Sb effectively suppressed the defect-related recombination. Meanwhile, the average emission lifetime of npn-SnS (4.16 ns) is longer than that of p-SnS (2.69 ns), indicating that npn-SnS has a longer carrier lifetime. Fig. 3c plots the incident photoelectron conversion efficiencies (IPCE) of npn-SnS and p-SnS. Note that the IPCE onset wavelength of npn-SnS is around 900 nm, corresponding to a band gap of 1.37 eV, which is consistent with the Tauc plot. Importantly, the value of npn-SnS is much higher than that of p-SnS, with a maximum value of 73 % at 430 nm, implying that Sn vacancies and Sb doping enhance the charge

carrier separation/transfer efficiency. The IPCE values of npn-SnS are much higher than all SnS-based photoelectrodes, strongly indicating the superiority of npn-SnS.

The PEC performance of npn-SnS and p-SnS photocathodes was evaluated by a three-electrode system under AM 1.5 G simulated sunlight ( $100 \text{ mW cm}^{-2}$ ) and without cocatalyst. Fig. 4a shows the photocurrent-voltage (J-V) plots for different photocathodes. The photocurrent density of the p-SnS photocathode at 0 V vs RHE is  $0.83 \text{ mA cm}^{-2}$ . It is worth noting that the onset potential of the npn-SnS photocathode is more positive than that of p-SnS, a phenomenon caused by the tuning of the work function by Sb doping[52]. The photocurrent density of npn-SnS ( $3.3 \text{ mA cm}^{-2}$  at 0 V vs. RHE) is approximately 4 times that of p-SnS, indicating the enhanced photoactivity of the npn-SnS photocathode. Most importantly, the fill factor of the J-V curve is significantly improved after doping with Sb. The improved fill factor of npn-SnS indicates that defect-related recombination is greatly suppressed by Sb doping, consistent with the PL spectroscopy results[53]. The stability of the photoelectrode is crucial for the photoelectrochemical reaction, so we further evaluated the stability of npn-SnS by long-term photocurrent-time (I-T) tests. After 8 h of testing, the vibration of the photocurrent of npn-SnS is negligible (Fig. 4b), and it remains at 93.0 % of the initial value even after 20 h (Fig. S18). In contrast, the photocurrent of the p-SnS photocathode exhibits abrupt decay. The SEM image after the p-SnS stability test is shown in Fig. S19, it can be seen that the p-SnS photocathode has obvious collapse. We conducted a more detailed study of the stability of npn-SnS (Fig. S20). SEM images illustrate that npn-SnS retains its original morphology after durability testing without any collapse. The corresponding XRD patterns also show no obvious peak shifts or phase transitions, indicating the excellent stability of npn-SnS. TEM, FFT, and HRTEM images also show no obvious change in the structure of npn-SnS. Meanwhile, as can be seen from Tables S3 and S4, the ICP results of the material after the three times PEC water splitting tests are not different, which fully illustrates the stability of the material. The XPS results after the reaction are not obviously different from those before the reaction, which also strongly illustrates the stability of the material (Fig. S21). The good structural stability of npn-SnS nanosheets may be due to the compact structure caused by the interaction between Sb and S. At the same time, doping Sb in the lattice of SnS also improves the stability of npn-SnS. To further confirm that the continuous photocurrent of the npn-SnS photocathode originates from a stable unity-Faradaic-efficiency hydrogen and oxygen evolution process, the evolved hydrogen and oxygen contents were quantified by gas chromatography (Fig. 4c). The amount of hydrogen and oxygen produced by npn-SnS and the counter electrode within 6 h is  $164.1$  and  $336.6 \text{ } \mu\text{mol cm}^{-2}$ , respectively, further confirming the excellent activity and robust stability of the npn-SnS photocathode. In addition, the continuous generation of  $\text{O}_2$  and  $\text{H}_2$  with Faradaic efficiencies approaching 100 % indicates that the photocurrent of the photocathode is entirely used for gas evolution. Furthermore, we evaluated the PEC performance of npn-SnS containing different Sb

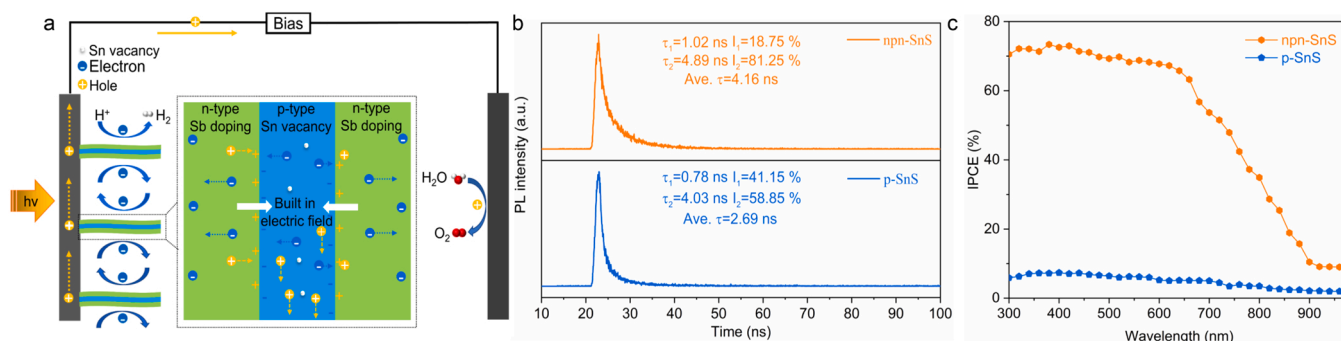
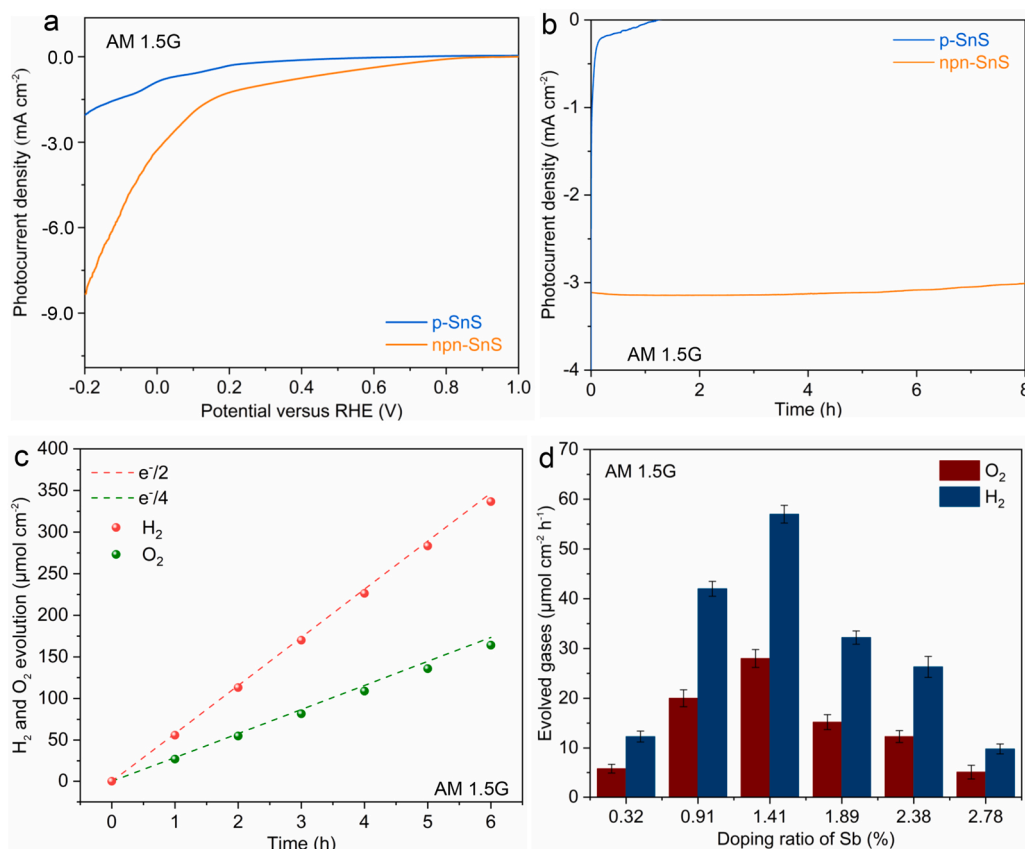


Fig. 3. a) Sketch of the sandwiched n-p-n homojunctions in npn-SnS. b) The TRPL decay spectra of npn-SnS and p-SnS. c) The IPCE spectrum of npn-SnS and p-SnS.



**Fig. 4.** a) The J-V plots of p-SnS and npn-SnS. b) Long-term photocurrent-time curves of p-SnS and npn-SnS. c) Amount of H<sub>2</sub> and O<sub>2</sub> generated from the npn-SnS photocathode and counter electrode under AM 1.5 G, and calculated gases from the photocurrent assuming 100 % Faradaic efficiency. d) H<sub>2</sub> and O<sub>2</sub> evolution amount in different Sb doping SnS. The test time is 1 h. Error bars are the standard deviation.

concentrations (Fig. 4d), showing the volcano type and revealing the optimal atomic ratio of Sb/Sb+Sn+S is about 1.41 %. The reason for the optimal atomic ratio of 1.41 % may be that most of Sb is doped into the outermost two layers, forming an npn homojunction with the inner layer containing Sn vacancies, which improves the performance.

To gain an advanced understanding of the photoelectrochemical activity of p-SnS and npn-SnS, we systematically investigated the catalytic performance of hydrogen reduction reactions (HER) on the catalyst surface. Here, we employ the method proposed by Nørskov et al. [54,55] to calculate the free energy change ( $\Delta G$ ) in HER (For detail, see supporting information). As shown in Fig. 5a and Fig. S22, we consider Sn-vacancy and Sb atom as active sites on p-SnS and npn-SnS, respectively. For HER process, the formation of  $\text{H}^*$ , involving the proton-coupled and electron-transfer ( $\text{H}^+ + \text{e}^- \rightarrow \text{H}^*$ ), is the rate-determining step as shown in Fig. 5b. It is worthy to note that  $\Delta G$  of npn-SnS (1.56 eV) is lower than that of p-SnS (3.24 eV), indicating that the npn-SnS can accelerate the HER. These results imply that npn-SnS has high activity for HER.

#### 4. Conclusion

In conclusion, we fabricated the thinnest sandwiched npn-SnS homojunction for the first time and explored its performance as an efficient photoelectrode for PEC water splitting. Structural characterization reveals that Sb doping and Sn vacancies are distributed on different layers, and the interaction between Sb and S makes npn-SnS possess the thinnest structure. Meanwhile, DFT calculations demonstrate that Sb doping can optimize the kinetics of HER and form a built-in electric field with Sn vacancies. The resultant npn-SnS possesses excellent structural stability and exhibits extraordinary PEC water

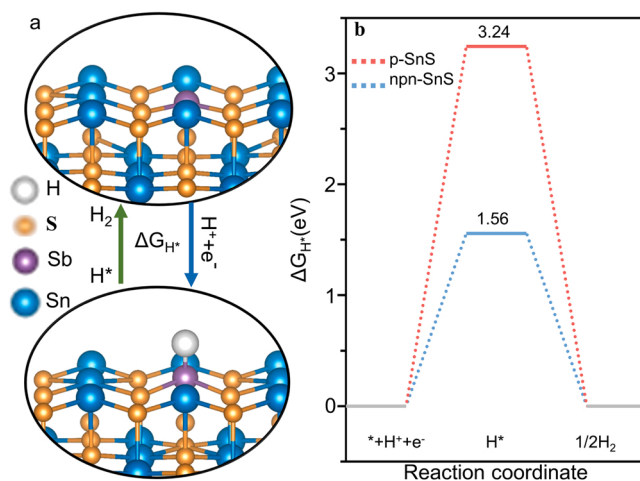


**Fig. 5.** a) Proposed pathways of hydrogen reduction reactions with the most energetically favorable absorbed intermediates ( $\text{H}^*$ ) in the Sb doping and Sn vacancy SnS. b) Free energy diagrams for the 2e pathways of hydrogen evolution reactions in the Sb doping and Sn vacancy SnS at pH = 7.

splitting performance. This work sheds light on the synthesis of ultrathin semiconductors and paves the way for the synthesis and application of high-performance SnS.

#### Declaration of Competing Interest

The authors declare that they have no known competing financial

interests or personal relationships that could have appeared to influence the work reported in this paper.

## Data Availability

Data will be made available on request.

## Acknowledgments

This work was financially supported by the Fundamental Research Funds for the Central Universities (0301005202017, 2018CDQYFXCS0017, 106112017CDJXSYY0001), Thousand Young Talents Program of the Chinese Central Government (Grant No. 0220002102003), National Natural Science Foundation of China (NSFC, Grant No. U19A20100, 21971027, 21373280, 21403019), Beijing National Laboratory for Molecular Sciences (BNLMS) and Hundred Talents Program at Chongqing University (Grant No. 0903005203205), The State Key Laboratory of Mechanical Transmissions Project (SKLMT-ZZKT-2017M11), Natural Science Foundation of Chongqing (Grant No. cstc2019jcyjmsxmX0426), Science and Technology Research Project of Education Agency in Chongqing (Grant No. KJZD-K201800102).

## Appendix A. Supporting information

Supplementary data associated with this article can be found in the online version at [doi:10.1016/j.apcatb.2022.122182](https://doi.org/10.1016/j.apcatb.2022.122182).

## References

- T. Takata, J. Jiang, Y. Sakata, M. Nakabayashi, N. Shibata, V. Nandal, K. Seki, T. Hisatomi, K. Domen, Photocatalytic water splitting with a quantum efficiency of almost unity, *Nature* 581 (2020) 411–414, <https://doi.org/10.1038/s41586-020-2278-9>.
- Y. Qiu, J. Zhou, Z. Liu, X. Zhang, H. Han, X. Ji, J. Liu, Solar-driven photoelectron injection effect on MgCo<sub>2</sub>O<sub>4</sub>@WO<sub>3</sub> core-shell heterostructure for efficient overall water splitting, *Appl. Surf. Sci.* 578 (2022), 152049, <https://doi.org/10.1016/j.apsusc.2021.152049>.
- L. Zhang, J. Wang, P. Liu, J. Liang, Y. Luo, G. Cui, B. Tang, Q. Liu, X. Yan, H. Hao, M. Liu, R. Gao, X. Sun, Ni(OH)<sub>2</sub> nanoparticles encapsulated in conductive nanowire array for high-performance alkaline seawater oxidation, *Nano Res.* 15 (2022) 6084–6090, <https://doi.org/10.1007/s12274-022-4391-6>.
- Y. Qiu, Z. Liu, X. Zhang, A. Sun, X. Ji, J. Liu, Controllable atom implantation for achieving Coulomb-force unbalance toward lattice distortion and vacancy construction for accelerated water splitting, *J. Colloid Inter. Sci.* 610 (2022) 194–201, <https://doi.org/10.1016/j.jcis.2021.12.029>.
- Z. Longcheng, L. Jie, Y. Luchao, D. Kai, L. Jun, Z. Donglin, L. Zerong, S. Shengjun, L. Yongsong, L. Qian, C. Guanwei, A.A. Abdulmohsen, G. Xiaodong, S. Xuping, Benzoate anions-intercalated NiFe-layered double hydroxide nanosheet array with enhanced stability for electrochemical seawater oxidation, *Nano Res. Energy* (2022), <https://doi.org/10.26599/NRE.2022.9120028>.
- C. Ye, L. Zhang, L. Yue, B. Deng, Y. Cao, Q. Liu, Y. Luo, S. Lu, B. Zheng, X. Sun, A NiCo LDH nanosheet array on graphite felt: an efficient 3D electrocatalyst for the oxygen evolution reaction in alkaline media, *Inorg. Chem. Front.* 8 (2021) 3162–3166, <https://doi.org/10.1039/d1qi00428j>.
- Q. Liu, S. Sun, L. Zhang, Y. Luo, Q. Yang, K. Dong, X. Fang, D. Zheng, A.A. Alshehri, X. Sun, N. O-doped carbon foam as metal-free electrocatalyst for efficient hydrogen production from seawater, *Nano Res.* 15 (2022) 8922–8927, <https://doi.org/10.1007/s12274-022-4869-2>.
- X. Sheng, T. Xu, X. Feng, Rational design of photoelectrodes with rapid charge transport for photoelectrochemical applications, *Adv. Mater.* 31 (2019), 1805132, <https://doi.org/10.1002/adma.201805132>.
- Y. Xiao, C. Feng, J. Fu, F. Wang, C. Li, V.F. Kunzelmann, C.-M. Jiang, M. Nakabayashi, N. Shibata, I.D. Sharp, K. Domen, Y. Li, Band structure engineering and defect control of Ta<sub>3</sub>N<sub>5</sub> for efficient photoelectrochemical water oxidation, *Nat. Catal.* 3 (2020) 932–940, <https://doi.org/10.1038/s41929-020-00522-9>.
- G. Wu, B. Tian, L. Liu, W. Lv, S. Wu, X. Wang, Y. Chen, J. Li, Z. Wang, S. Wu, H. Shen, T. Lin, P. Zhou, Q. Liu, C. Duan, S. Zhang, X. Meng, S. Wu, W. Hu, X. Wang, J. Chu, J. Wang, Programmable transition metal dichalcogenide homojunctions controlled by nonvolatile ferroelectric domains, *Nat. Electron.* 3 (2020) 43–50, <https://doi.org/10.1038/s41928-019-0350-y>.
- C. Liu, L. Wang, J. Qi, K. Liu, Designed growth of large-size 2D single crystals, *Adv. Mater.* 32 (2020), 2000046, <https://doi.org/10.1002/adma.202000046>.
- H. Zheng, Y. Lu, K.H. Ye, J. Hu, S. Liu, J. Yan, Y. Ye, Y. Guo, Z. Lin, J. Cheng, Y. Cao, Atomically thin photoanode of InSe/graphene heterostructure, *Nat. Commun.* 12 (2021) 91, <https://doi.org/10.1038/s41467-020-20341-7>.
- X. Yu, M.S. Prevot, N. Guijarro, K. Sivula, Self-assembled 2D WSe<sub>2</sub> thin films for photoelectrochemical hydrogen production, *Nat. Commun.* 6 (2015) 7596, <https://doi.org/10.1038/ncomms8596>.
- V.L. Nguyen, D.L. Duong, S.H. Lee, J. Avila, G. Han, Y.-M. Kim, M.C. Asensio, S.-Y. Jeong, Y.H. Lee, Author correction: layer-controlled single-crystalline graphene film with stacking order via Cu–Si alloy formation, *Nat. Nanotechnol.* 16 (2021) 114–116, <https://doi.org/10.1038/s41565-020-00821-z>.
- R. Li, X. Ma, J. Li, J. Cao, H. Gao, T. Li, X. Zhang, L. Wang, Q. Zhang, G. Wang, C. Hou, Y. Li, T. Palacios, Y. Lin, H. Wang, X. Ling, Flexible and high-performance electrochromic devices enabled by self-assembled 2D TiO<sub>2</sub>/MXene heterostructures, *Nat. Commun.* 12 (2021) 1587, <https://doi.org/10.1038/s41467-021-21852-7>.
- T.-N. Do, M. Idrees, B. Amin, N.N. Hieu, H.V. Phuc, L.T. Hoa, C.V. Nguyen, First principles study of structural, optoelectronic and photocatalytic properties of SnS, SnSe monolayers and their van der Waals heterostructure, *Chem. Phys.* 539 (2020), 110939, <https://doi.org/10.1016/j.chemphys.2020.110939>.
- E. Sutter, J. Wang, P. Sutter, Lateral heterostructures of multilayer GeS and SnS van der Waals Crystals, *ACS Nano* 14 (2020) 12248–12255, <https://doi.org/10.1021/acsnano.0c05978>.
- Y.G. Song, I.-H. Baek, J.-G. Yim, T. Eom, T.-M. Chung, C.-H. Lee, C.S. Hwang, C.-Y. Kang, S.K. Kim, Cross-linked structure of self-aligned p-type SnS nanoplates for highly sensitive NO<sub>2</sub> detection at room temperature, *J. Mater. Chem. A* 10 (2022) 4711–4719, <https://doi.org/10.1039/d1ta11014d>.
- J. Meng, J. Wang, J. Wang, Q. Li, J. Yang, β-SnS/GaSe heterostructure: a promising solar-driven photocatalyst with low carrier recombination for overall water splitting, *J. Mater. Chem. A* 10 (2022) 3443–3453, <https://doi.org/10.1039/d1ta10074b>.
- P. Sutter, H.P. Komsa, H. Lu, A. Gruverman, E. Sutter, Few-layer tin sulfide (SnS): controlled synthesis, thickness dependent vibrational properties, and ferroelectricity, *Nano Today* 37 (2021), 101082, <https://doi.org/10.1016/j.nantod.2021.101082>.
- H.Q. Yang, X.Y. Wang, H. Wu, B. Zhang, D.D. Xie, Y.J. Chen, X. Lu, X.D. Han, L. Miao, X.Y. Zhou, Sn vacancy engineering for enhancing the thermoelectric performance of two-dimensional SnS, *J. Mater. Chem. C* 7 (2019) 3351–3359, <https://doi.org/10.1039/c8tc05711g>.
- Z. Guo, Y. Wang, A. Elbourne, A. Mazumder, C.K. Nguyen, V. Krishnamurthi, J. Yu, P.C. Sherrell, T. Daeneke, S. Walia, Y. Li, A. Zavabeti, Doped 2D SnS materials derived from liquid metal-solution for tunable optoelectronic devices, *Nanoscale* 14 (2022) 6802–6810, <https://doi.org/10.1039/d2nr01135b>.
- Y. Sun, Z. Sun, S. Gao, H. Cheng, Q. Liu, F. Lei, S. Wei, Y. Xie, All-surface-atomic-metal chalcogenide sheets for high-efficiency visible-light photoelectrochemical water splitting, *Adv. Energy Mater.* 4 (2014), 1300611, <https://doi.org/10.1002/aenm.201300611>.
- V. Krishnamurthi, H. Khan, T. Ahmed, A. Zavabeti, S.A. Tawfik, S.K. Jain, M.J. S. Spencer, S. Balendhran, K.B. Crozier, Z. Li, L. Fu, M. Mohiuddin, M.X. Low, B. Shabbir, A. Boes, A. Mitchell, C.F. McConville, Y. Li, K. Kalantar-Zadeh, N. Mahmood, S. Walia, Liquid-metal synthesized ultrathin SnS layers for high-performance broadband photodetectors, *Adv. Mater.* 32 (2020), e2004247, <https://doi.org/10.1002/adma.202004247>.
- P. Li, H. Dong, J. Xu, J. Chen, B. Jiao, X. Hou, J. Li, Z. Wu, Ligand orientation-induced lattice robustness for highly efficient and stable Tin-Based perovskite solar cells, *ACS Energy Lett.* 5 (2020) 2327–2334, <https://doi.org/10.1021/acsenenergylett.0c00960>.
- M.P.A. Muthalif, Y. Choe, Control of the interfacial charge transfer resistance to improve the performance of quantum dot sensitized solar cells with highly electrocatalytic Cu-doped SnS counter electrodes, *Appl. Surf. Sci.* 508 (2020), 145297, <https://doi.org/10.1016/j.apsusc.2020.145297>.
- S. Dembele, A. Akcil, S. Panda, Technological trends, emerging applications and metallurgical strategies in antimony recovery from stibnite, *Miner. Eng.* 175 (2022), 107304, <https://doi.org/10.1016/j.mineng.2021.107304>.
- M. Seal, N. Singh, E.W. McFarland, J. Baltrusaitis, Electrochemically Deposited Sb and In Doped Tin Sulfide (SnS) Photoelectrodes, *J. Phys. Chem. C* 119 (2015) 6471–6480, <https://doi.org/10.1021/jp512927y>.
- R. Dahule, C.C. Singh, K. Hongo, R. Maezono, E. Panda, Anomalies in the bulk and surface electronic properties of SnS: effects of native defects, *J. Mater. Chem. C* 10 (2022) 5514–5525, <https://doi.org/10.1039/d1tc04738h>.
- G. Kresse, J. Furthmüller, Efficiency of ab-initio total energy calculations for metals and semiconductors using a plane-wave basis set, *Comp. Mater. Sci.* 6 (1996) 15–50, [https://doi.org/10.1016/0927-0256\(96\)00008-0](https://doi.org/10.1016/0927-0256(96)00008-0).
- G. Kresse, J. Furthmüller, Efficient iterative schemes for ab initio total-energy calculations using a plane-wave basis set, *Phys. Rev. B* 54 (1996) 11169–11186, <https://doi.org/10.1103/PhysRevB.54.11169>.
- M.C. Payne, M.P. Teter, D.C. Allan, T.A. Arias, J.D. Joannopoulos, Iterative minimization techniques for ab initio total-energy calculations: molecular dynamics and conjugate gradients, *Rev. Mod. Phys.* 64 (1992) 1045–1097, <https://doi.org/10.1103/RevModPhys.64.1045>.
- J. Klimes, D.R. Bowler, A. Michaelides, Chemical accuracy for the van der Waals density functional, *J. Phys. Condens. Matter* 22 (2010), 022201, <https://doi.org/10.1088/0953-8984/22/2/022201>.
- S. Nose, A unified formulation of the constant temperature molecular-dynamics methods, *J. Chem. Phys.* 81 (1984) 511–519, <https://doi.org/10.1063/1.447334>.
- J.K. Nørskov, J. Rossmeisl, A. Logadottir, L. Lindqvist, J.R. Kitchin, T. Bligaard, H. Jónsson, Origin of the overpotential for oxygen reduction at a fuel-cell cathode, *J. Phys. Chem. B* 108 (2004) 17886–17892, <https://doi.org/10.1021/jp047349j>.



- [36] Á. Valdés, Z.W. Qu, G.J. Kroes, J. Rossmeisl, J.K. Nørskov, Oxidation and photo-oxidation of water on TiO<sub>2</sub> surface, *J. Phys. Chem. C* 112 (2008) 9872–9879, <https://doi.org/10.1021/jp711929d>.
- [37] J. Rossmeisl, Z.W. Qu, H. Zhu, G.J. Kroes, J.K. Nørskov, Electrolysis of water on oxide surfaces, *J. Electro Chem.* 607 (2007) 83–89, <https://doi.org/10.1016/j.jelechem.2006.11.008>.
- [38] J. Greeley, T.F. Jaramillo, J. Bonde, I. Chorkendorff, J.K. Nørskov, Computational high-throughput screening of electrocatalytic materials for hydrogen evolution, *Nat. Mater.* 5 (2006) 909–913, <https://doi.org/10.1038/nmat1752>.
- [39] R. Johnson, 2013. NIST Computational Chemistry Comparison and Benchmark Database, (2013).
- [40] J. Huang, Y. Ma, K. Yao, C. Wu, M. Cao, J. Lai, J. Zhang, Y. Sun, Linjun Wang, Y. Shen, Chemical bath deposition of SnS:In thin films for Pt/CdS/SnS:In/Mo photocathode, *Surf. Coat. Technol.* 358 (2019) 84–90, <https://doi.org/10.1016/j.surfcoat.2018.11.025>.
- [41] M. Cao, K. Yao, C. Wu, J. Huang, W. Yang, L. Zhang, F. Lei, Y. Sun, L. Wang, Y. Shen, Facile synthesis of SnS and SnS<sub>2</sub> nanosheets for FTO/SnS/SnS<sub>2</sub>/Pt photocathode, *ACS Appl. Energy Mater.* 1 (2018) 6497–6504, <https://doi.org/10.1021/acsaelm.8b01414>.
- [42] W. Fu, Y. Wang, W. Tian, H. Zhang, J. Li, S. Wang, Y. Wang, Non-Metal single-phosphorus-atom catalysis of hydrogen evolution, *Angew. Chem. Int. Ed. Engl.* 59 (2020) 23791–23799, <https://doi.org/10.1002/anie.202011358>.
- [43] S. Man, H. Bao, K. Xu, H. Yang, Q. Sun, L. Xu, W. Yang, Z. Mo, X. Li, Preparation and characterization of Nd-Sb co-doped SnO<sub>2</sub> nanoflower electrode by hydrothermal method for the degradation of norfloxacin, *Chem. Eng. J.* 417 (2021), 129266, <https://doi.org/10.1016/j.cej.2021.129266>.
- [44] X. Ren, X. Zhang, N. Liu, L. Wen, L. Ding, Z. Ma, J. Su, L. Li, J. Han, Y. Gao, White light-emitting diode from Sb-Doped p-ZnO nanowire Arrays/n-GaN film, *Adv. Funct. Mater.* 25 (2015) 2182–2188, <https://doi.org/10.1002/adfm.201404316>.
- [45] C. Cao, X. Xie, Y. Zeng, S. Shi, G. Wang, L. Yang, C.-Z. Wang, S. Lin, Highly efficient and stable p-type ZnO nanowires with piezotronic effect for photoelectrochemical water splitting, *Nano Energy* 61 (2019) 550–558, <https://doi.org/10.1016/j.nanoen.2019.04.098>.
- [46] W. Wang, T. Zhang, A. Seliverstov, H. Zhang, Y. Wang, F. Wang, X. Peng, Q. Lu, C. Qin, X. Pan, Y.-J. Zeng, C. Van Haesendonck, Z. Ye, Layer-dependent optoelectronic properties of 2D van der Waals SnS grown by pulsed laser deposition, *Adv. Electron Mater.* 6 (2020), 1901020, <https://doi.org/10.1002/aelm.201901020>.
- [47] L. Meng, J. He, W. Tian, M. Wang, R. Long, L. Li, Ni/Fe codoped In<sub>2</sub>S<sub>3</sub> nanosheet arrays boost photo-electrochemical performance of planar Si photocathodes, *Adv. Energy Mater.* 9 (2019), 1902135, <https://doi.org/10.1002/aenm.201902135>.
- [48] Y. Wu, X. Liu, H. Zhang, J. Li, M. Zhou, L. Li, Y. Wang, Atomic sandwiched p-n Homojunctions, *Angew. Chem. Int. Ed. Engl.* 60 (2021) 3487–3492, <https://doi.org/10.1002/anie.202012734>.
- [49] T. Jia, F. Fu, J. Li, Z. Deng, F. Long, D. Yu, Q. Cui, W. Wang, Rational construction of direct Z-scheme SnS/g-C<sub>3</sub>N<sub>4</sub> hybrid photocatalyst for significant enhancement of visible-light photocatalytic activity, *Appl. Surf. Sci.* 499 (2020), <https://doi.org/10.1016/j.apsusc.2019.143941>.
- [50] Y. Liu, Y. Cai, G. Zhang, Y.-W. Zhang, K.-W. Ang, Al-Doped black phosphorus p-n homojunction diode for high performance photovoltaic, *Adv. Funct. Mater.* 27 (2017), 1604638, <https://doi.org/10.1002/adfm.201604638>.
- [51] X. Zhan, Y. Zheng, B. Li, Z. Fang, H. Yang, H. Zhang, L. Xu, G. Shao, H. Hou, W. Yang, Rationally designed Ta<sub>3</sub>N<sub>5</sub>/ZnIn<sub>2</sub>S<sub>4</sub> 1D/2D heterojunctions for boosting Visible-Light-driven hydrogen evolution, *Chem. Eng. J.* 431 (2022), 134053, <https://doi.org/10.1016/j.cej.2021.134053>.
- [52] K.H. Ye, H. Li, D. Huang, S. Xiao, W. Qiu, M. Li, Y. Hu, W. Mai, H. Ji, S. Yang, Enhancing photoelectrochemical water splitting by combining work function tuning and heterojunction engineering, *Nat. Commun.* 10 (2019) 3687, <https://doi.org/10.1038/s41467-019-11586-y>.
- [53] D. Bartsaghi, C. Perez Idel, J. Kniepert, S. Roland, M. Turbiez, D. Neher, L. J. Koster, Competition between recombination and extraction of free charges determines the fill factor of organic solar cells, *Nat. Commun.* 6 (2015) 7083, <https://doi.org/10.1038/ncomms8083>.
- [54] J.K. Nørskov, J. Rossmeisl, Logadottir, L. Lindqvist, J.R. Kitchin, T. Bligaard, H. Jonsson, Origin of the overpotential for oxygen reduction at a fuel-cell cathode, *J. Phys. Chem. B* 108 (2004) 17886–17892.
- [55] J. Rossmeisl, Z.W. Qu, H. Zhu, G. Kroes, J.K. Nørskov, Electrolysis of water on oxide surfaces, *J. Electroanal. Chem.* 607 (2007) 83–89.